Effects of Phase Purity and Pore-Reinforcement on Mechanical Behavior of NU-1000 and Silica-Infiltrated NU-1000 Metal-Organic Frameworks

Zhao Wang,^{1,†} Kevin M. Schmalbach,^{2,†} Rebecca L. Combs,¹ Youxing Chen,³ R. Lee Penn,¹ Nathan A. Mara,^{2,*} Andreas Stein^{1,*}

¹ Department of Chemistry, University of Minnesota, 207 Pleasant St SE, Minneapolis, Minnesota 55455, USA

² Department of Chemical Engineering and Materials Science, University of Minnesota, 421 Washington Ave SE, Minneapolis, Minnesota 55455, USA

³ Department of Mechanical Engineering, UNC Charlotte, 9201 University City Blvd., Charlotte, North Carolina 28223, USA

Keywords: Metal-organic frameworks, NU-1000, silica-reinforced NU-1000, nanocasting, nanoindentation, finite element simulation

[†] These authors contributed equally to this work.

ABSTRACT: Metal-organic framework (MOF) materials have shown promise in many applications, ranging from gas storage to absorption and catalysis. Because of the high porosity and low density of many MOFs, densification methods such as pelletization and extrusion are needed for practical use and for commercialization of MOF materials. Therefore, it is important to elucidate the mechanical properties of MOFs and to develop methods of further enhancing their mechanical strength. Here we demonstrate the influence of phase purity and the presence of a porereinforcing component on elastic modulus and yield stress of NU-1000 MOFs through nanoindentation methods and finite-element simulation. Three types of NU-1000 single crystals were compared: phase-pure NU-1000 prepared with biphenyl-4-carboxylic acid as a modulator (NU-1000-bip), NU-1000 prepared with benzoic acid as a modulator (NU-1000-ben), which results in an additional, denser impurity phase of NU-901, and NU-1000-bip whose mesopores were infiltrated with silica (SiO_x(OH)_v@NU-1000) by nanocasting methods. By maintaining phase purity and minimizing defects, the elastic modulus could be enhanced by nearly an order of magnitude: phase-pure NU-1000-bip crystals exhibited an elastic modulus of 20 GPa whereas the value for NU-1000-ben crystals was only 3 GPa. The introduction of silica into the mesopores of NU-1000-bip did not strongly affect the measured elastic modulus, but significantly increased the load at failure from 2000 μ N to 3000–4000 μ N.

1. INTRODUCTION

Metal–organic frameworks (MOFs) are a class of porous materials composed of metal ions or oxo-metal clusters and organic "linker" molecules. ¹⁻⁴ In MOFs, the organic linkers act as the bridging ligands that connect numerous metal ion/oxo-metal cluster nodes, forming a periodic, porous structure. Many MOFs feature high surface areas and uniform pore structures. Additionally, due to the extraordinary flexibility in the choice of building blocks, the number of possible MOF materials with different topologies and pore dimensions is very large. Over 88,000 different structures have been reported in the MOF-subset of the Cambridge Structural Database, among which more than 8,000 are porous, ⁵ with pore diameters up to 9.8 nm, pore volumes reaching 5.0 cm³/g, and BET surface areas as high as 7839 m²/g. ⁶⁻¹¹ Because of their structural and compositional diversity, MOFs have shown promise in many applications, including gas storage, chemical separation, catalysis, and sensors. ¹²⁻¹⁸

However, for practical use and commercialization of MOFs, it may be necessary to densify and pelletize these high porosity, low density materials in processes that require high pressures. Therefore, in addition to their chemical properties, the mechanical properties of MOFs are another important criterion to assess whether a MOF is suitable for practical applications. Understanding the behavior of MOF materials under mechanical stress can facilitate the design and screening of robust MOFs for specific purposes. A few publications reported the influence of external pressure on certain chemical and structural properties of MOFs, such as phase transitions,¹⁹ bond breakage,²⁰ and pore structure collapse.²¹⁻²² Additionally, Moghadam et al. studied the structure-mechanical property relationships for 3,385 MOFs using high-throughput molecular mechanics calculations.²³ However, direct studies of the mechanical properties of MOFs remain challenging because many MOF materials consist of particles smaller than 1 μm, which makes them hard to

manipulate and characterize by traditional mechanical testing methods.²⁴⁻²⁵ To date, studies on the mechanical properties of MOFs have been mainly performed on thin-film coatings and single crystals through traditional nanoindentation techniques.²⁶⁻²⁹ Recently, an atomic force microscopy (AFM)-based nanoindentation technique was applied to MOFs.³⁰ With this method, mechanical data could be acquired for MOFs with even smaller particle sizes (< 500 nm).³⁰ Elastic moduli and hardness values of some typical MOF materials are summarized in **Table 1**.

Table 1. Elastic modulus and hardness of some MOF materials determined by nanoindentation.^a

| MOF | form | Young's modulus | hardness | indenter tip |
|---------|------------------------------|-----------------|-------------------|--------------|
| | | (GPa) | (GPa) | |
| HKUST-1 | thin film ²⁶ | 9.3 | 0.23 ± 0.04 | Berkovich |
| | thin film ²⁷ | 3.5 ± 2.5 | 0.17 ± 0.16 | Berkovich |
| ZIF-8 | single crystal ²⁸ | 3.2 ± 0.1 | 0.50 ± 0.02 | Berkovich |
| | single crystal ³⁰ | ~3 | ~0.5 | AFM-based |
| IRMOF-1 | single crystal ²⁹ | 2.7 ± 1.0 | 0.058 ± 0.026 | Berkovich |
| UiO-66 | nanoparticle ²⁴ | 22–45 | N.A. | AFM-based |
| UiO-67 | single crystal ³¹ | 20.0 | 1.27 | Berkovich |

^aThis table shows a selection of the most common MOF materials whose mechanical properties have been investigated. These properties can be modulated by manipulating the species of clusters and linkers. For example, when the zirconium atoms in the clusters of UiO-66 are substituted for hafnium, the elastic modulus increases from 22–45 to 30–60 GPa, because the Hf–O bond is stronger than the Zr–O bond.²⁴ By incorporating more sterically bulky linkers, the elastic modulus of ZIF MOFs can be increased from 3 to 10 GPa.²⁸

Tan et al. reported a map of elastic modulus vs. hardness for major classes of materials, including metals, ceramics, polymers, and hybrid framework materials.³² From their results, MOFs

mostly exhibit elastic moduli in the 1–30 GPa range and hardness values in the 0.02–2 GPa range. One interesting finding in their research is that the MOF region in the map overlaps with the intersection of regions for polymers, metals, and ceramics, indicating the potential of MOFs to substitute for traditional materials when specific properties are preferred, such as ordered structure or large porosity. Notably, as organic–inorganic hybrid materials, MOFs do not have intrinsically high mechanical strength compared to other well-known porous materials consisting of inorganic building units. For example, the elastic moduli of silicalite-1 and ZSM-5 are 40 GPa and 57 GPa, respectively, larger than those of the MOFs listed in **Table 1**.³² Additionally, many other types of dense organic-inorganic hybrid materials can also outperform MOFs in terms of elastic modulus and hardness. For example, copper phosphonoacetate and cerium oxalate-formate hybrid materials show elastic moduli as high as 90 GPa and 78 GPa, respectively.³³⁻³⁴ However, MOFs have their unique structural advantages, including very low density, high surface area, uniform and ordered pores, all of which are attractive for many purposes. Therefore, elucidation of the mechanical properties of MOF materials is important for paving the way for their future commercialization.

The functionality of MOFs relies to a large extent on their open pore structures and unsaturated clusters.³⁵⁻³⁹ In other words, high porosity and low connectivity between clusters and linkers are desired for a MOF material to be competitive. However, these properties also result in low density and possibly lower stability, which compromise the mechanical properties of MOFs.⁴⁰ One possible approach to address these competing tendencies is to introduce reinforcing components into the pores of MOFs while still leaving enough open space or maintaining the clusters unsaturated. To date, very few papers have been published regarding this topic.

Robison et al. reported a method to enhance the bulk modulus of NU-901 at the expense of increasing the connectivity of the clusters from 8 to 10 (still leaving 2 unsaturated sites for each

cluster).²⁵ Malonzo et al. and Zhao et al. reported the partial filling of the pores of NU-1000 with amorphous silica, titania, or polymer, which maintained 48–77% of its original porosity.⁴¹⁻⁴² However, the mechanical properties were not studied after introducing the reinforcing phases.

NU-1000 is a relatively thermally stable, mesoporous MOF, which consists of oxo-zirconium clusters ("Zr₆" clusters, [Zr₆(μ_3 -O)₄(μ_3 -OH)₄(OH)₄(OH)₄(OH)₂|⁸⁺) and 1,3,6,8-tetrakis(p-benzoate)pyrene (TBAPy⁴⁻) linkers.⁴³ The Zr₆ clusters are in the shape of an octahedron with each triangular face capped with μ_3 -O or μ_3 -OH groups.⁴⁴ This rigid structure with high symmetry endows NU-1000 with superior chemical and thermal stabilities compared to many other MOFs.⁴ Another advantage of NU-1000 is the unsaturated nature of the Zr₆ clusters, in which only eight out of the twelve edges in the Zr₆-octahedron are connected with linkers.³⁵ The unoccupied sites in the Zr₆ clusters make NU-1000 a good substrate for further modifications, which extends its application range in catalysis, CO₂ adsorption, and remediation of toxins.^{17, 38, 45-46}

In earlier studies of NU-1000, another phase, NU-901 was typically present as an impurity at a fraction of ~20% on the basis of a single-crystal X-ray diffraction analysis. NU-1000 and NU-901 are both composed of Zr₆ clusters with 8-fold connectivity by the TBAPy⁴⁻ linkers. However, their structures differ topologically. The Zr₆ clusters in NU-1000 are aligned at an angle of 60° relative to each other, whereas they are positioned parallel to each other in NU-901. This topology change reduces the largest pore size from 3.1 nm in NU-1000 to 1.2 nm in NU-901 and increases the density of the MOF. The presence of an NU-901 impurity also alters the morphology of NU-1000 particles and can result in twinning. The NU-901 phase is typically present at mid-length of the NU-1000 particles. The key for the achievement of phase-pure MOFs was later found to be the use of appropriate modulators. Modulators are molecules that usually have the same functional group as the linkers but only on one side (monodentates). They adjust the reaction

kinetics via capping the clusters at the beginning and slowly releasing them to connect with the linkers. The equilibrium between the modulator-capped clusters and linkers regulates the MOF crystal growth.⁵⁰ The inclusion of an NU-901 phase can be inhibited by replacing benzoic acid as a modulator by larger biphenyl-4-carboxylic acid molecules, which causes stronger steric interactions between the capped metal clusters during their assembly.⁴⁸ As a result, the rotation of the C–C bond and Zr₆ clusters is prevented, avoiding the formation of the NU-901 phase (**Figure 1**).

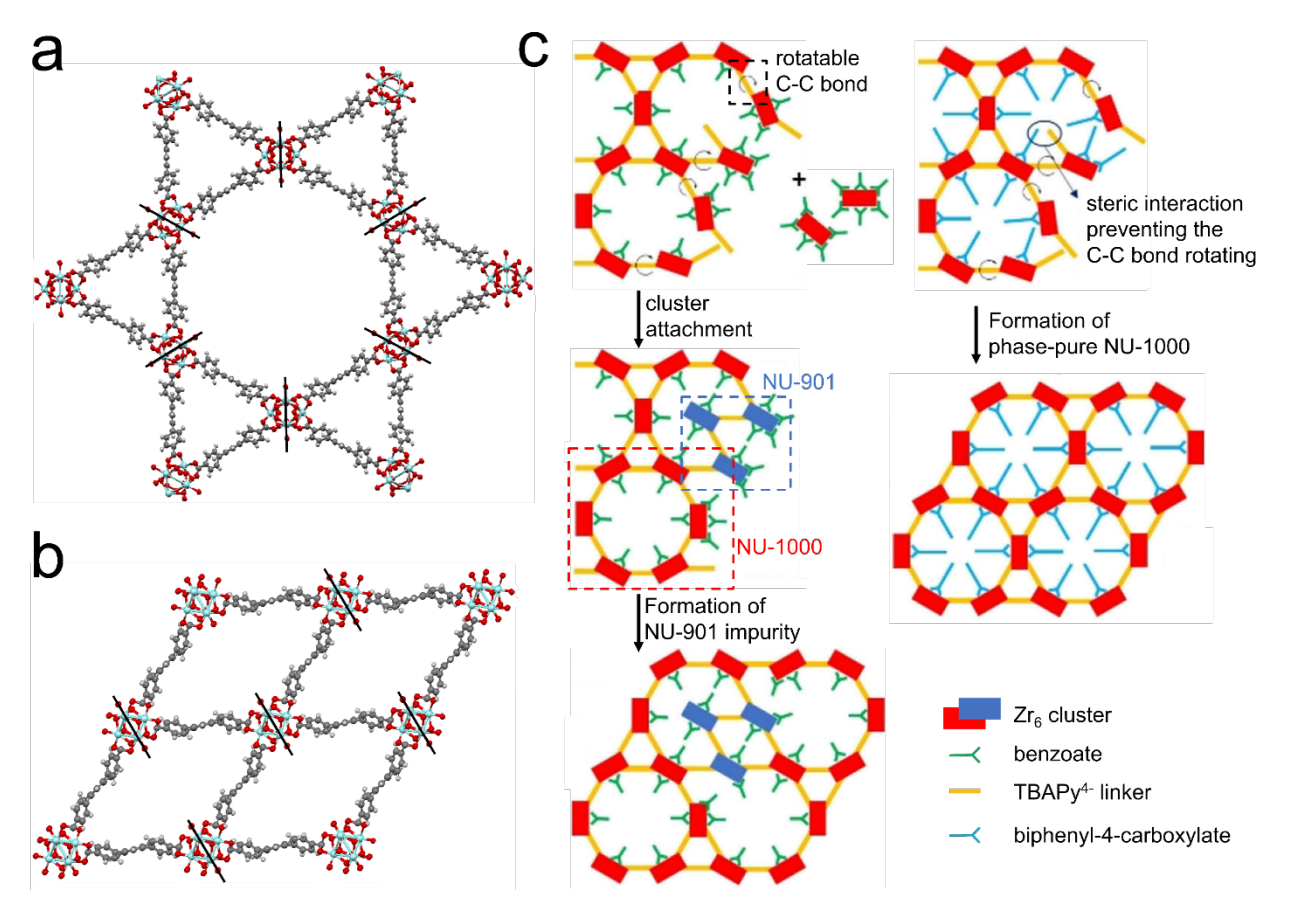


Figure 1. Structures of (a) NU-1000 and (b) NU-901. Both MOFs are composed of Zr₆ clusters and TBAPy⁴⁻ linkers. However, the clusters in NU-1000 are aligned at 60° relatively to each other whereas in NU-901 all clusters are aligned in parallel. In addition, NU-1000 has two types of pores (3.1 nm and 1.1 nm), but NU-901 only has one type (1.2 nm). Color code: Zr (blue); red (oxygen); C (grey); H (white). (c) Scheme showing the formation of NU-901 inside NU-1000 using benzoic acid as the modulator and the prevention of NU-901 forming with biphenyl-4-carboxylic acid as the modulator. Part (c) was adapted with permission from ref. 45, Copyright (2017), American Chemical Society.

Here we compare the effects of phase purity and an internal reinforcing phase on mechanical properties of NU-1000 by nanoindentation and finite-element simulation. Three types of NU-1000 single crystals were compared: phase-pure NU-1000 prepared with biphenyl-4-carboxylic acid as a modulator (NU-1000-bip), NU-1000 prepared with benzoic acid as a modulator (NU-1000-ben), which results in an additional, denser impurity phase of NU-901, and NU-1000-bip whose mesopores were infiltrated with silica ($SiO_x(OH)_y@NU-1000$) by nanocasting methods. These last

materials have previously been applied to provide thermal stabilization for Zr₆ clusters for high-temperature applications.^{41-42, 46, 51} This comparison provides insight into the effects of non-intentional and intentional secondary phases on the mechanical properties of NU-1000.

2. EXPERIMENTAL METHODS

- **2.1. Materials.** Chemicals used in this study were obtained from the following sources: 1,3,6,8-tetrakis(p-benzoic acid)pyrene (H₄TBAPy) synthesized by the Hupp and Farha groups at Northwestern University via a previously reported method;³⁵ ethanol (anhydrous, 200 proof) from Pharmco-AAPER; N,N-diethylformamide (DEF, certified ACS, 99.9%), acetone (certified ACS, 99.7%) from Fisher Chemical; tetramethyl orthosilicate (98%), methanol (>99.8%), hydrochloric acid (ACS reagent, 37%), zirconium(IV) chloride (≥ 99.9%) from Sigma-Aldrich; biphenyl-4-carboxylic acid (98%) from Alfa Aesar; sodium hydroxide (99%) from Riedel-de Haën. Deionized water was used in all syntheses after purification to a minimum resistivity of 18.2 M Ω ·cm with a Milli-Q PLUS reagent-grade water system.
- **2.2. Synthesis of NU-1000.** Two types of NU-1000 were used in this study, each synthesized with a different modulator. The NU-1000 synthesized using benzoic acid as modulator was denoted as NU-1000-ben. The synthesis of NU-1000-ben followed a previously reported method.⁴³ The NU-1000 synthesized using biphenyl-4-carboxylic acid was denoted as NU-1000-bip. NU-1000-bip was synthesized as follows. Biphenyl-4-carboxylic acid (6.343 g, 32.00 mmol) and ZrCl₄ (139.8 mg, 0.60 mmol) were added into 16 mL of *N*,*N*-diethylformamide (DEF) and heated at 100 °C for 1 h. The Zr₆ clusters capped with biphenyl-4-carboxylic acid were obtained in this process. To prepare the linker suspension, H₄TBAPy acid (100 mg, 0.15 mmol) was suspended in 1.5 mL of DEF using sonication for better dispersion. An amount of 14.6 μL (0.015 mmol) of 1 M NaOH

was then added to the linker suspension. The linker suspension was finally added to the suspension of the Zr_6 clusters. The mixture was heated at 100 °C for 48 h and then cooled down to room temperature. It was centrifuged at 9,000 rpm for 10 min, the supernatant was discarded, and the precipitate was dissolved with fresh DEF. This washing step was repeated twice. After the final washing step, the precipitate was suspended in 16 mL of fresh DEF. This suspension was mixed with 1 mL of 8 M HCl solution, which was then heated at 80 °C for 20 h. The reaction mixture was cooled to room temperature and centrifuged at 9,000 rpm for 10 min. The precipitate was washed three times with DEF and three times with acetone. Particles were left to dry overnight under air. This synthesis produced particles with lengths up to 10 μ m. When the amounts of all synthesis components were cut in half, particles with lengths up to 2.5 μ m were formed. The phasepure NU-1000 is denoted as NU-1000-bip in the following text. Composition of NU-1000-ben: $Zr_{1.0}C_{14.6}H_{11.4}O_{5.7}$, composition of NU-1000-bip: $Zr_{1.0}C_{13.0}H_{11.3}O_{5.4}$, theoretical composition for both: $Zr_{1.0}C_{14.7}H_{10.0}O_{5.3}$.

2.3. Synthesis of SiO_x(OH)_y@NU-1000. Silica-infiltrated NU-1000 was synthesized following a published method.⁴¹ Volumes of 100 μL of deionized water and 180 μL of methanol were added into 600 μL of tetramethyl orthosilicate (TMOS). The mixture was sonicated for 10 min and then added to 30 mg of activated NU-1000. The infiltration of TMOS into NU-1000 was allowed to proceed for 24 h hours for batches with particle sizes up to 2.5 μm and 40, 80 or 100 h for batches with particle sizes up to 10 μm. The infiltrated MOF was then washed twice with methanol to remove any TMOS remaining on the external surface of the NU-1000 particles. The mixture was heated at 50 °C for 5 min to dry, and then exposed to HCl vapor for 24 h at room temperature in order to induce the condensation of TMOS. The mixture was then heated at 80 °C for 24 h. The resulting product was denoted as SiO_x(OH)_y@NU-1000.

- **2.4. Preparation of segregated dispersed particles for mechanical testing.** A spatula tip of NU-1000 or $SiO_x(OH)_y@NU$ -1000 particles was dispersed in 2 mL of acetone. The mixture was sonicated for 10 min. One drop of the dispersion was added onto a silicon wafer (0.5 cm × 0.5 cm). After the acetone evaporated, isolated individual particles were present on the silicon wafer. The silicon wafer was then attached to an SEM stub with Super Glue.
- **2.5.** Characterization methods. FT-IR spectra were obtained in transmission mode on a Nicolet Magna 760 IR spectrometer, using powdered samples compressed between a pair of NaCl windows. Powder X-ray diffraction patterns were collected using a PANalytical X'Pert Pro diffractometer. The X-rays were generated with a Co anode (K α radiation, $\lambda = 1.789$ Å) which operated at 45 kV accelerating voltage, 40 mA emission current. ¹H nuclear magnetic resonance (NMR) spectra were recorded on a Bruker Ascend AV-500 spectrometer at room temperature. Nitrogen sorption experiments were performed on a Quantachrome Autosorb-iQ2 analyzer using ultrahigh purity grade nitrogen adsorptive. All samples were degassed under dynamic vacuum (0.003 mTorr) at 120 °C for 12 h before analyses. Brunauer–Emmett–Teller (BET) surface areas were evaluated from the adsorption isotherms in the relative pressure range 0.01–0.20. Scanning electron microscopy (SEM) was performed on a JEOL-6500 field emission scanning electron microscope with an accelerating voltage of 5.0 kV. Scanning electron microscopy combined with energy-dispersive X-ray spectroscopy (SEM-EDS) was conducted on a JEOL JXA-8900 electron probe microanalyzer with an Ultradry-SDD detector and an accelerating voltage of 15.0 kV to 20 kV. All samples were coated with a 50 Å platinum film prior to SEM imaging or a 70 Å carbon film for EDS analyses. Transmission electron microscopy (TEM) measurements were obtained using a FEI Tecnai T12 transmission electron microscope with an accelerating voltage of 120 kV and a LaB₆ filament. Samples were sonicated for 5 min in ethanol and then deposited onto carbon

film-coated copper grids. Scanning transmission electron microscopy—energy dispersive X-ray spectroscopy (STEM-EDS) was performed using an FEI Tecnai G2 field-emission S/TEM operating at an accelerating voltage of 80 kV. Samples were loaded onto 300-mesh lacey carbon/Cu TEM grids by drop-casting a dilute suspension of each sample in acetone. High-angle annular dark field (HAADF) images were collected on an E. A. Fischione annular detector using an inner collection semi-angle of 25.5 mrad. Energy-dispersive X-ray spectroscopy (EDS) spectra were obtained using the ChemiSTEM EDX spectrometer. EDS maps were collected while rastering the beam over the sample, which minimized beam damage. A probe current of ~0.8 nA was used, and maps were collected over a minimum of 5 min. Data were analyzed using ESPRIT software (version 1.9.4). Thermogravimetric analysis (TGA) was performed on a TA Instruments Q500 TGA in air with a heating rate of 5 °C/min to estimate the Zr content in the samples from the residual mass (ZrO₂). The analyses of carbon and hydrogen content in the samples were carried out by Atlantic Microlab, Norcross, GA.

- **2.6. Nanoindentation.** The mounted sample was placed in a Hysitron PI88 *in situ* nanoindenter (Bruker Nano Surfaces, Minneapolis, MN) equipped with an xR low load transducer and a 20 μm diameter diamond flat punch probe. A minimum of three *in situ* compression experiments were conducted in an FEI Helios G4 UX FIB/SEM (Thermo Fisher Scientific) operated at 2 kV. The indenter was operated in displacement control mode with a displacement rate of 15 nm/s.
- 2.7. Finite element analysis. Compression along the flat face of the hexagonal cross section of the particles produces a non-uniform stress state in the particle. To quantify the average properties in the cross section, finite element modeling was performed using Abaqus/Standard (Dassault Systems). A two-dimensional regular hexagonal planar cross section (height of 1 μm for NU-1000-bip, height of 2 μm for NU-1000-ben) was compressed using CPS3 plane stress nodes. Although

the bulk of the material in the experiments is not expected to be strictly in a plane stress condition, the Poisson's ratio is expected to be low, making this a reasonable approximation. Only the initial loading of the MOF particles was modeled to approximate the elastic properties. These models assumed a dense, elastically isotropic material. The elastic modulus input was varied to produce load–displacement curves for the elastic region of the loading (**Figure S2**). Each modulus corresponds to a characteristic measured stiffness in the elastic regime; the stiffness (slope of the load–displacement curve) was determined for each simulation to prepare a calibration curve (**Figure S3**) relating the stiffness and the elastic modulus, as known from the simulation. The elastic portion of each experiment was then fit with a line to measure the stiffness (slope) and used in the calibration curve to determine the elastic modulus.

Once elastic properties were determined, isotropic plastic properties were added to the model. The starting guess for the yield stress was the average stress in the particle, as determined from the elastic simulation, at the end of the linear elastic loading regime. To model the plasticity as elastic—perfectly plastic, a table of yield stress was input with a work hardening rates of 0.5 GPa for NU-1000-bip and 0.05 GPa for NU-1000-ben. In a similar manner to the elastic case, several simulations were run, this time varying the yield stress of the particle. Rather than having a characteristic stiffness, different yield stresses have characteristic failure loads (**Figure S4**). The characteristic load was determined by the intersection of a line fitting the elastic regime and a line fitting the linear response of the plastic behavior and plotted against the known yield stress to make another calibration curve (**Figure S5**). The same process was applied to the experimental data to infer the yield stress of the material.

3. RESULTS AND DISCUSSION

3.1. Structure and composition of the NU-1000 and SiO_x(OH)_v@NU-1000 materials

Whereas NU-1000-ben contains NU-901 as an impurity phase, this impurity was eliminated in NU-1000-bip by changing the modulator from benzoic acid to biphenyl-4-carboxylic acid during the synthesis. The structural differences between these two materials were previously reported.⁴⁸ Structural and compositional properties of the NU-1000-ben and NU-1000-bip materials used here were characterized by multiple methods, including SEM (Figure S1), N₂ sorption (Figure S6, **Table S1**), XRD (**Figure S7**), TGA and CHN analysis (**Figure S8**). The morphology of NU-1000 particles changed as the impurity phase was removed. Webber et al. had previously shown that NU-1000-ben was denser near the middle of the particles, which resulted in TEM phase contrast that was not seen in NU-1000-bip (Figure S1a, b). 48 Here, SEM images revealed that NU-1000ben crystals are narrower at mid-length and usually display twinning on the external surface of the rods, whereas phase-pure NU-1000 crystals have a straight rod shape with a hexagonal crosssection and smoother surfaces (Figure S1c, d). NU-1000-ben and NU-1000-bip both exhibited high surface areas and porosity (Figure S6a, Table S1). Although the powder XRD patterns of these samples in the low-angle region (Figure S7) could not distinguish between the NU-1000 and NU-901 phases, the N₂ sorption isotherms showed clear differences in the micropore and mesopore regions (Figure S6a). The isotherm for NU-1000-bip showed the features of both micropores (relative pressure $P/P_0 < 0.1$) and mesopores ($P/P_0 > 0.5$), which are also apparent in the pore size distribution curve (Figure S6b). The peak at 1.2 nm corresponds to the smaller, triangular micropores and the peak at 2.7 nm corresponds to the larger hexagonal mesopores (see **Figure 1**). The isotherm for NU-ben indicates a greater N₂ volume adsorbed at low relative pressure and a slightly lower volume at high relative pressure; in addition, the peak at 2.7 nm is reduced in intensity compared to that at 1.2 nm. Compared to NU-1000-bip, NU-1000-ben contains a larger fraction of micropores due to the NU-901 impurity phase, which only has micropores. On the basis

of the change in micropore fraction, the fraction of NU-901 in NU-1000-ben was estimated to be about 20%, consistent with the value reported from single crystal analysis (see **Table S1**).³⁵

Because MOF materials are highly porous, it was hypothesized that with extra reinforcing material introduced into their pores, the overall mechanical properties of the material could be enhanced. The feasibility of introducing different materials into the pores of MOFs has been reported elsewhere. 42, 51 In this study, TMOS was introduced into the pores of NU-1000 after extensive washing with DEF and acetone, which ensured that either benzoic acid or biphenyl-4carboxylic acid modulators were almost completely removed from the MOF particles (Figure S9). This was followed by hydrolysis and condensation of TMOS by exposing the infiltrated particles to HCl vapor. The infiltration of TMOS into the pores was facilitated by capillary forces (NU-1000 was preheated under vacuum to evacuate the air and water from the pores). After the infiltration process, the material was washed with methanol to remove any remaining TMOS from the external surface of the NU-1000 particles. Because the materials were dried at a relatively low temperature of 60 °C, the embedded silica still contained a large fraction of hydroxyl groups. Therefore, the reinforcing material formed inside the pores was denoted as $SiO_x(OH)_v$, and the whole material was denoted as $SiO_x(OH)_v @ NU-1000$. To focus on the role of the reinforcing phase on mechanical properties without influence from any NU-901 phase impurity, the introduction of $SiO_x(OH)_v$ was only performed on NU-1000-bip in this study.

Structural details of $SiO_x(OH)_y@NU-1000$ -ben were reported in our previous publication (the structure was referred to as $SiO_2@NU-1000$). It was observed that after the infiltration of silica into NU-1000-ben, the specific surface area, pore volume, and pore diameter decreased (from 2064 to 901 m²/g, 1.44 to 0.55 cm³/g, and 2.7 to 2.2 nm, respectively), indicating the presence of silica

inside the pores of NU-1000-ben. In addition, silica was found to occupy mainly the 3.1 nm mesopores on the basis of gas sorption and difference envelope density analyses.

The textural characteristics of the $SiO_x(OH)_v @NU-1000$ -bip system were similar to those observed for $SiO_x(OH)_v @ NU-1000$ -ben, confirming the incorporation of silica in the pores of NU-1000-bip. After infiltration with silica, the specific surface area of NU-1000-bip decreased from 1905 to 1292 m²/g and the pore volume from 1.19 to 0.73 cm³/g (Table S1). The pore size distribution curve calculated from N₂ sorption measurements (Figures 2a and S10) showed a significant decrease in intensity for the larger mesopores with a shift from 2.7 to 2.3 nm, while the peak at 1.2 nm corresponding to the small micropores maintained its position. These results indicated that the introduced silica mainly occupied the larger mesopores, similar to what was reported for $SiO_x(OH)_v(@NU-1000$ -ben. At this point it is not known how the silica interacts with the oxozirconium clusters. A possible binding site for silica in NU-1000 would be the -OH groups on the zirconium oxide clusters to form Si-O-Zr bonds. Corresponding Si-O-Zr vibrations would exhibit IR signals in the 963-980 cm⁻¹ range.⁵²⁻⁵³ While no IR peaks were observed for $SiO_x(OH)_y$ @NU-1000-bip in this range (**Figure S11**), the possibility of silica-oxozirconium cluster interactions cannot be excluded, given the relatively high silica: Zr ratio in these materials (Table S2).

Changes in the XRD patterns of NU-1000-bip and silica infiltrated NU-1000-bip (**Figure 2b**) also paralleled observations for $SiO_x(OH)_y@NU-1000$ -ben. Major peaks of NU-1000 were still observed after the infiltration except for the (100) peak at 3°. The (100) planes in NU-1000 cut through the larger hexagonal mesopores and the decreased intensity of this peak for the $SiO_x(OH)_y@NU-1000$ -bip sample results from the reduction in electron contrast as the hexagonal

pores are partially filled with silica. Other peaks are broadened after infiltration of NU-1000-bip with silica.

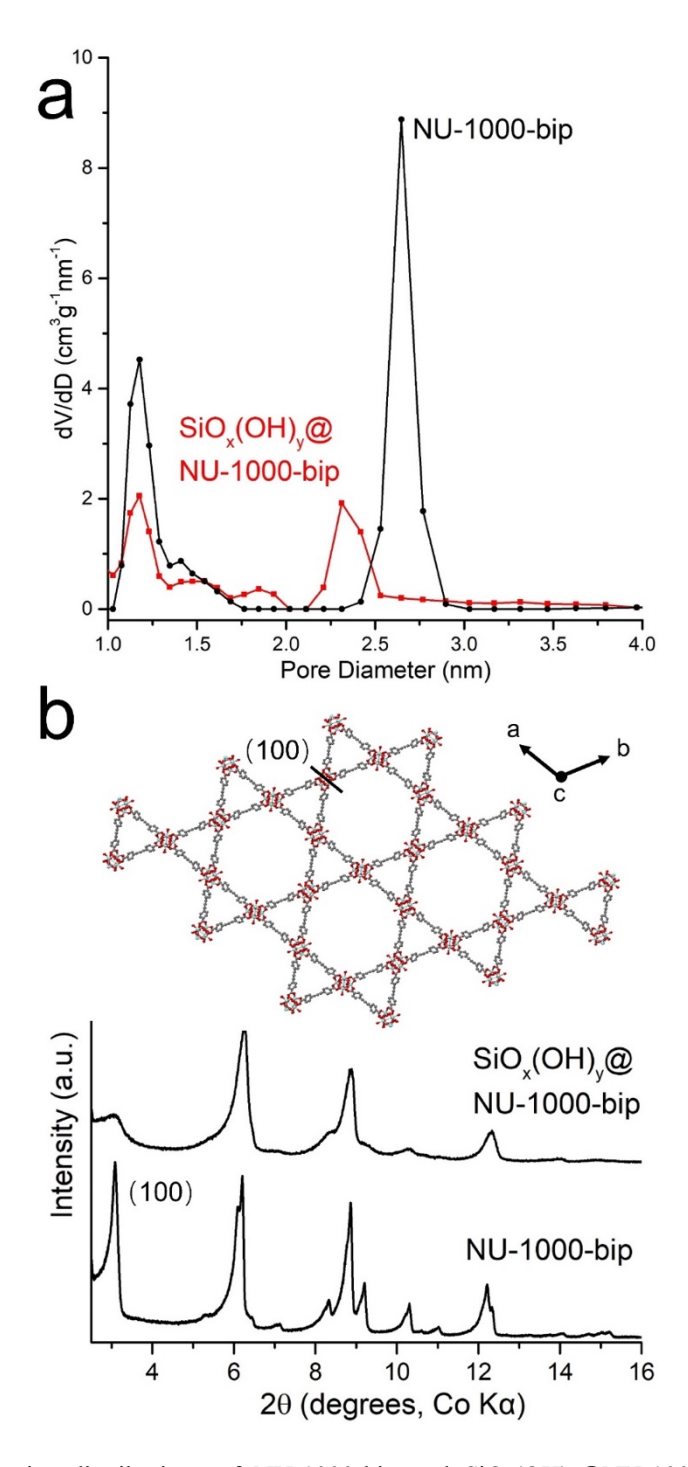


Figure 2. (a) DFT pore size distributions of NU-1000-bip and $SiO_x(OH)_y@NU-1000$ -bip samples. Pore size distributions were calculated by NLDFT using a slit pore model. (b) XRD patterns of NU-1000-bip and $SiO_x(OH)_y@NU-1000$ -bip materials. The inset in (b) illustrates the (100) plane in NU-1000.

In contrast, the distribution of silica throughout individual $SiO_x(OH)_y@NU-1000$ -bip and $SiO_x(OH)_y@NU-1000$ -ben particles differed, as revealed by STEM-EDS maps. While Si was distributed uniformly throughout $SiO_x(OH)_y@NU-1000$ -bip particles (**Figure S12b**), the Si concentration near the middle of $SiO_x(OH)_y@NU-1000$ -ben particles typically deviated from the remaining areas of the particles (**Figure S12a**). This behavior supported the location of the NU-901 phase impurity in $SiO_x(OH)_y@NU-1000$ -ben and the absence of such an impurity in $SiO_x(OH)_y@NU-1000$ -bip. No external silica crust was observed in either sample.

For mechanical testing, we aimed to use the largest possible particles of NU-1000-bip and SiO_x(OH)_y@NU-1000-bip. For NU-1000 particles up to 2.5 μm in length, an infiltration time of 24 h was suitable to achieve efficient infiltration with a silica scaffold.⁴¹ However, in the present study, for the application of the silica infiltration method to the more defect-free NU-1000-bip material, the influence of infiltration time on composite structure was re-evaluated, considering the facts that: (1) unlike NU-1000-ben, NU-1000-bip contains purely the NU-1000 phase, so the fraction of 3.1 nm pores is larger; and (2) larger NU-1000 particles (~10 μm in length) would be expected to require a longer time for diffusion of TMOS through the particle. Three different infiltration times were investigated: 40, 80, and 100 h, and the extent of infiltration was evaluated by comparing characteristic FT-IR absorptions of silica to those of NU-1000 (**Figure S11a**).

In the FT-IR spectra, peaks at 1417 and 1100 cm⁻¹ correspond to the asymmetric vibration of COO⁻ and stretching vibrations of Si–O–Si, respectively. The COO⁻ peak is representative of the presence of TBAPy⁴⁻ linkers, and Si–O–Si indicates the presence of silica. Because the number of linkers did not change during the infiltration process, the peak area ratio of $v_{\text{(Si-O-Si)}}/v_{\text{(COO-)}}$ is an indication of the relative content of silica in SiO_x(OH)_y@NU-1000-bip. These ratios were 1.4, 1.6, and 1.7 for samples infiltrated for 40, 80, and 100 h, indicating that more silica was introduced

with longer infiltration time. This result was consistent with SEM-EDS data, which revealed increasing Si/Zr₆ ratios from 23, 29, and 34 for the NU-1000-bip samples infiltrated with TMOS for 40 h, 80 h, and 100 h (**Table S2**). It is noted that in a previous study of infiltrating smaller particles of modified NU-1000 with silica, the Si/Zr₆ ratio surpassed $50.^{46}$ Therefore, the Si/Zr₆ ratio in this study might be further increased with infiltration times longer than 100 h. The SiO_x(OH)_y@NU-1000-bip-100h material which contained the largest amount of silica was selected for mechanical testing, considering that it should show the greatest impact of the secondary phase on mechanical properties.

SEM images confirmed that the morphology of NU-1000-bip was maintained even after long infiltration with TMOS in the $SiO_x(OH)_y@NU-1000$ -bip-100h particles (**Figure 3a, b**). Rodshaped particles were still observed with no evidence for any extraneous silica particles formed on the outside if the infiltrated particles, which was ensured by the washing process to remove any remaining TMOS after the infiltration process. Further evidence for the absence of an external silica layer around the NU-1000 was provided by contrast analysis of a TEM image of $SiO_x(OH)_y@NU-1000$ -bip-100h (**Figure 3c**).

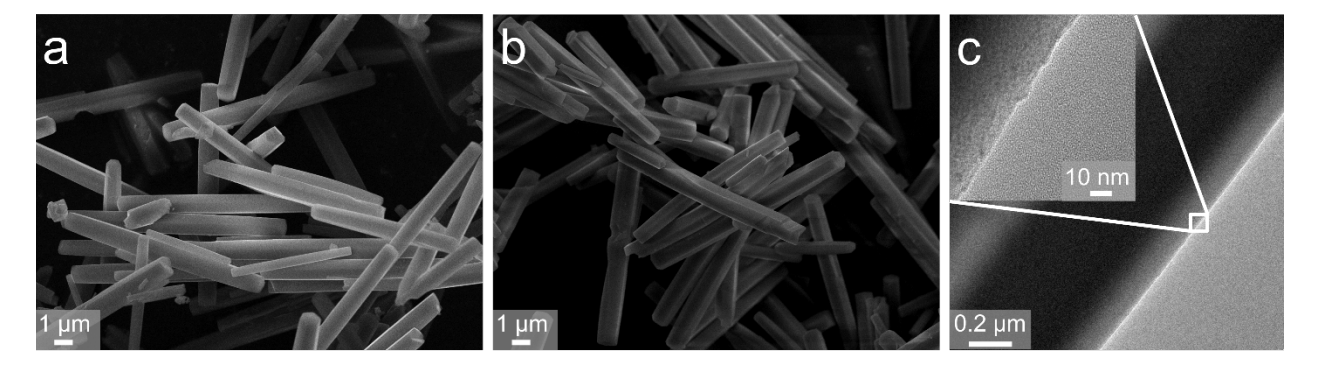


Figure 3. SEM images of (a) NU-1000-bip and (b) $SiO_x(OH)_y$ @NU-1000-bip-100h. (c) TEM image of $SiO_x(OH)_y$ @NU-1000-bip-100h.

To investigate the mechanical properties of the NU-1000 and the SiO_x(OH)_y@NU-1000 particles, it is important to keep them separated as single particles in order to prevent particle stacking which would complicate the mechanical analysis. To obtain highly dispersed particles on a substrate, small amounts of NU-1000 or SiO_x(OH)_y@NU-1000 materials were dispersed in acetone. After sonication, the dispersion was dropped onto silicon wafers. Separate, well-dispersed particles were left on the silicon substrate after the acetone evaporated (**Figure 4**). The average dimensions (length/width) of the particles were measured to be $9.5 \pm 0.5 \,\mu\text{m}/2.3 \pm 0.3 \,\mu\text{m}$ for NU-1000-ben, $10.5 \pm 2.0 \,\mu\text{m}/1.1 \pm 0.2 \,\mu\text{m}$ for NU-1000-bip, and $10.8 \pm 1.8 \,\mu\text{m}/1.1 \pm 0.2 \,\mu\text{m}$ for SiO_x(OH)_y@NU-1000-bip-100h (6 separate rods were measured for each sample).

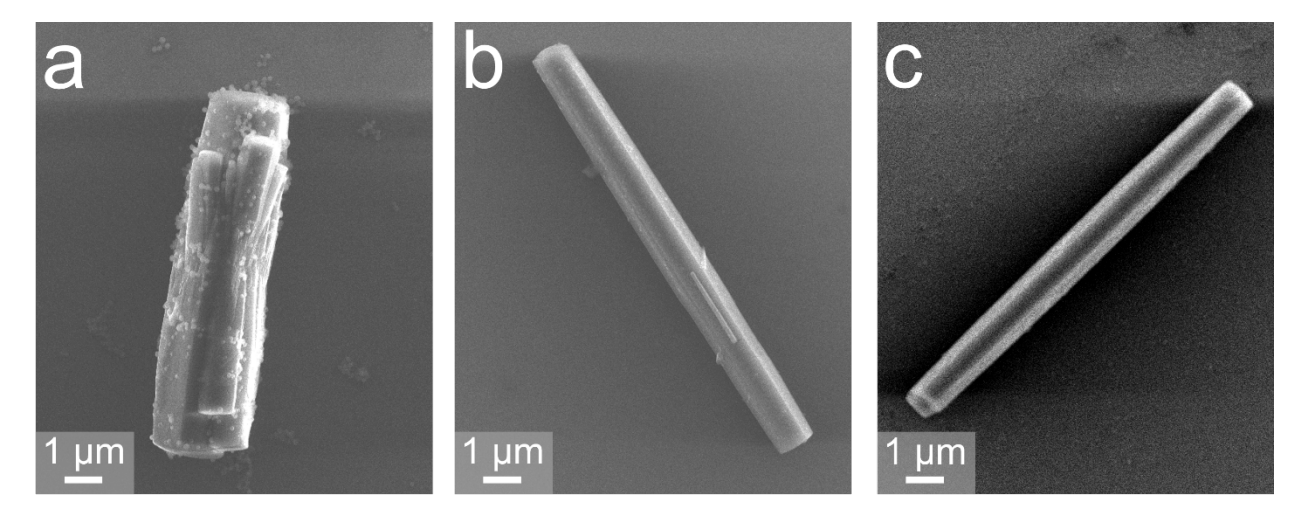


Figure 4. SEM images of (a) NU-1000-ben, (b) NU-1000-bip, and (c) SiO_x(OH)_y@NU-1000-bip-100h particles.

3.2. Mechanical testing of NU-1000 and SiO_x(OH)_v@NU-1000

In a linear elastic material, the initial load-displacement response is expected to be linear. At the beginning of a compression test, there is occasionally a non-linear "foot" prior to the linear response due to a small misalignment between the indenter probe and the sample, such that the full contact area is not established all at once, leading to a variable loading slope. After the linear

loading response, a deviation from linearity typically indicates some type of permanent deformation, such as plastic deformation or fracture.

NU-1000 and $SiO_x(OH)_y@NU$ -1000-bip particles were compressed under the indenter. The height of the particles decreased from 1.2 to 0.5 µm for NU-1000-bip, 1.1 to 0.5 µm for $SiO_x(OH)_y@NU$ -1000-bip-100h, and 2.0 to 1.2 µm for NU-1000-ben (**Figure 5**). None of the three particles fractured under compression, implying their good fracture resistance in the direction parallel to the hexagonal cross-section.

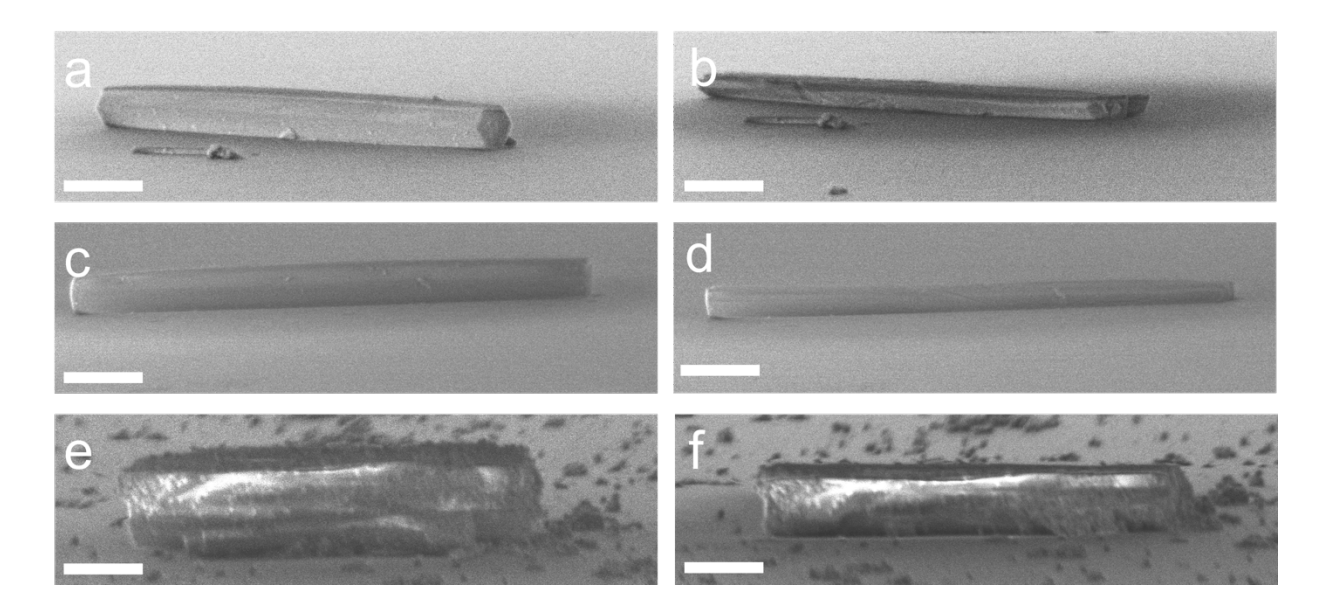


Figure 5. SEM images of NU-1000-bip, $SiO_x(OH)_y@NU-1000$ -bip-100h, and NU-1000-ben particles before compression (a, c, e) and after compression (b, d, f) under the indenter. Small extraneous particles seen around the indented particle in (f) were also present on the precursor sample in (e). They were not identified and are not believed to influence the measurements. The scale bar in all images corresponds to 2 μ m.

The compressive load–displacement curves of each particle can be seen in **Figure 6a**. To qualitatively compare the three materials, one can compare the slope of the loading curve, or the loading stiffness, after contact has been established. The loading stiffness of the NU-1000-bip and $SiO_x(OH)_y@NU-1000$ -bip are comparable, both exceeding the loading stiffness of NU-1000-ben.

The point of deviation from linearity, which will be considered the point of failure, was determined by inspection of the load-displacement response. The point of failure for the three materials is significantly different. NU-1000-bip fails at approximately 2000 µN, approximately 4 times higher than the phase-impure NU-1000-ben. In contrast, the phase-pure, silica-infiltrated material $(SiO_x(OH)_v @ NU-1000-bip)$ fails at loads 50–100% higher than the non-infiltrated NU-1000-bip, between 3000 and 4000 µN. At these loads, some structural failure occurs. Although the deformation mechanism is not presently known, it is likely linked to pore collapse within the structure. Here, pore collapse is defined broadly, and more investigation is needed to determine the relative contribution of organic ligament bending versus fracture or catastrophic pore collapse. This would also explain why the load-displacement curve of $SiO_x(OH)_v(@NU-1000$ -bip does not exhibit a load drop until later; in this case, the coating of silica on the interior of the pores carries a fraction of the load, allowing the material to elastically deform until a higher load is reached, at which the embedded silica, too, would fail, causing a decrease in the measured stiffness. Of note is that "nominal strain to failure", or the indenter displacement divided by the particle height at the point of failure, is approximately equal (~0.1) for both NU-1000-bip and NU-1000-ben, again indicating that this is the maximum possible strain that the framework structure of the MOF can undergo prior to pore collapse, and thus indicating a reduced measured stiffness.

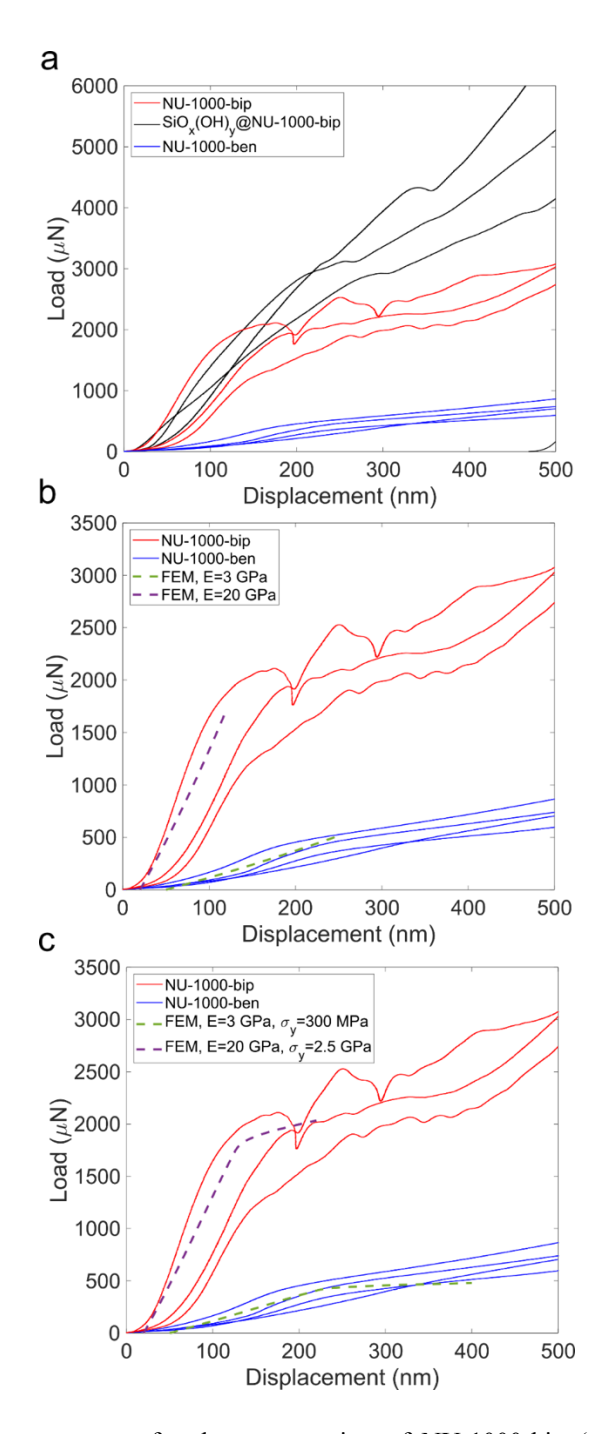


Figure 6. (a) Load–displacement curves for the compression of NU-1000-bip (red), NU-1000-ben (blue), and $SiO_x(OH)_y@NU-1000$ -bip (black). NU-1000-bip and $SiO_x(OH)_y@NU-1000$ -bip have significantly higher stiffness than NU-1000-ben. (b) Load–displacement curves from (a) plotted on a smaller scale. Overlaid are the simulated load–displacement curves from finite element modeling (FEM) assuming elastic moduli (E) of 20 GPa (purple) and 3 GPa (green). (c) Load–displacement curves from (b) incorporating an elastic–perfectly plastic solution using a yield stress, σ_y , of 2.5 GPa for NU-1000-bip and 300 MPa for NU-1000-ben.

3.3. Finite element simulation

In an effort to quantify the effective elastic modulus of NU-1000 and $SiO_x(OH)_v @NU-1000$ materials, the loading of a hexagonal planar section of material was simulated in Abaqus/Standard. The load-displacement output of the simulation is overlaid on the experimental load-displacement curves in **Figure 6**. A displacement offset was added to the simulation output to partially overcome the initial increase in slope due to the establishment of full contact with the particle. Now, rather than comparing the apparent stiffness of the particles, it is possible to compare the effective loading modulus. Using the range of simulations performed and the calibration curve method described above, one can infer the elastic modulus from each test. Doing so determines an average elastic modulus of 21 GPa for NU-1000-bip with a standard deviation of 3.7 GPa. It should be noted that the standard deviation is high, partially due to the limited number of experiments performed. Additionally, the average elastic modulus of $SiO_x(OH)_v @NU-1000$ -bip was calculated to be 19 GPa with a standard deviation of 3.9 GPa. Load-displacement data from simulations with corresponding elastic moduli overlaid can be seen in **Figure 6b**. Because the loading slopes are so similar with large standard deviations, the elastic moduli of the two materials cannot presently be distinguished. In contrast, the average elastic modulus of NU-1000-ben was calculated to be 3.2 GPa with a standard deviation of 0.7 GPa. The load-displacement response from simulation with this elastic modulus also qualitatively compares to that of NU-1000-ben (Figure 6b); this elastic modulus is well within the range of previously recorded values.^{28, 54} Note that the slope of the loading curve in compression experiments is typically lower than the elastic modulus. The effective elastic moduli that are simulated with this method are therefore expected to be lower bounds for the true effective elastic moduli. Here, the elastic modulus of NU-1000-bip is higher than the values measured via Berkovich nanoindentation of ZIF single crystals (3-9 GPa) or HKUST-1 thin films (9.3 GPa).^{26, 28} DFT calculations have determined the elastic modulus of IRMOF-1 to be ~21 GPa.²⁹ However, a more suitable comparison may be between experiments with a similar loading state (simple compression), rather than sharp tip indentation. One such comparison can be made to the *in situ* compression of UiO-type MOFs, which also contain Zr₆ clusters; the unloading moduli of UiO-type MOFs were measured to be 20–80 GPa,⁵⁴ in better agreement with the modulus inferred from the compression and modeling reported here. The higher modulus of UiO-type MOFs likely results from their higher connectivity of the linkers to the Zr₆ clusters, e.g., 12 for UiO-66 and UiO-67 compared to 8 for NU-1000.

In addition to the determination of the elastic moduli of the particles, the simulations were also able to elucidate the distribution of stress within the particles at the point of load excursion/failure (Figure 7). As expected, high stresses are observed at the top and bottom vertices of the hexagon. However, the stresses are very low toward the other vertices which are not under direct loading. More importantly, the stresses are not limited merely to the volume between the top and bottom vertices, but they exhibit some lateral spread, confirming that stress should not be assumed to be the load divided by the area in contact with the indenter tip. The point of deviation from linearity, which will be considered the point of failure, was determined by inspection of the load–displacement response. At the point of failure in NU-1000-bip, the von Mises stress within the bulk of the particle is on the order of 2.5 GPa, whereas the von Mises stress at failure for NU-1000-ben is much lower, on the order of 300 MPa. As noted earlier, at this stress, some structural failure occurs. Although the deformation mechanism is not presently known, it is likely linked to pore collapse within the structure. Again, pore collapse is defined broadly here until future investigations into detailed failure mechanisms can be conducted. The internal stresses at the point

of failure provide a convenient initial estimate for the yield/failure stress in additional simulations using an elastic–perfectly plastic model.

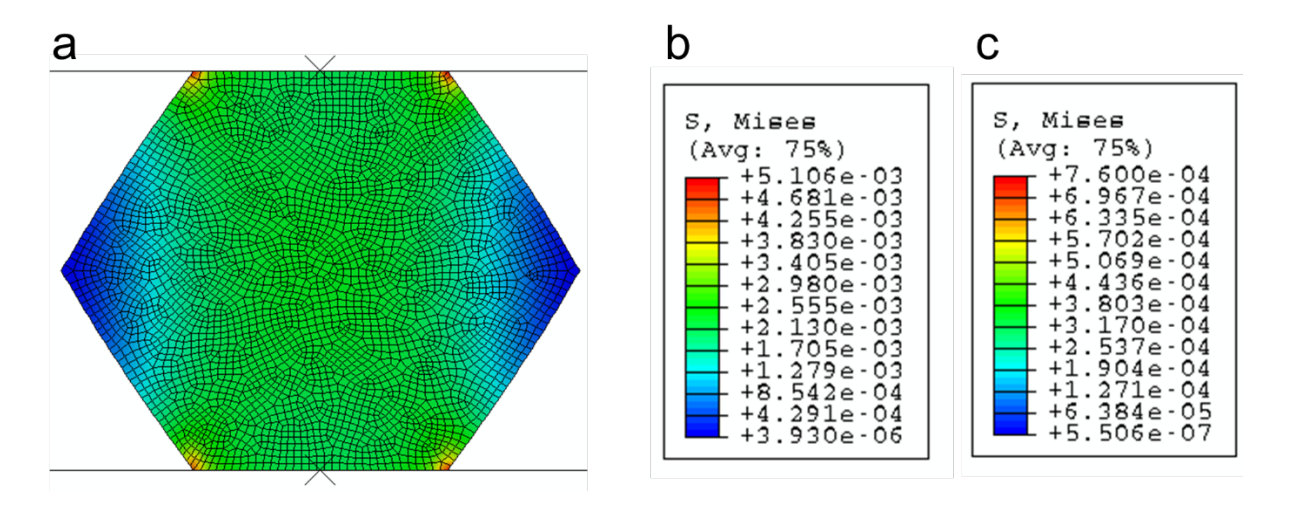


Figure 7. (a) The shape of the stress distribution at the point of failure assuming isotropic elasticity. Colors correspond to stress contours for (b) NU-1000-bip and (c) NU-1000-ben. Stresses are von Mises stresses with units of TPa. Bulk stress at failure is approximately 2.5 GPa for NU-1000-bip and 300 MPa for NU-1000-ben.

In an elastic-plastic model, the material first undergoes elastic deformation, as in the previous simulations, but begins to yield once the material reaches its yield stress. The slope of the load-displacement curve post-failure was very low in some cases, which implies elastic-perfectly plastic behavior. To be perfectly plastic means that no work hardening occurs, i.e., no additional stress is required to continue to deform the yielded material. To implement this in Abaqus requires a low slope for the plastic behavior; this was chosen arbitrarily to be 0.5 GPa for NU-1000-bip and 0.05 GPa for NU-1000-ben. A factor of 2 difference in work hardening rate results in minute changes in the stresses in the particle.

As stated previously, the stress in the particle at the point of failure from the purely elastic simulations was used as an initial estimate for the yield stress in the elastic-plastic simulations. Again, several simulations were performed in the vicinity of this yield stress to create a curve

relating the characteristic failure load and the known yield stress. The results of the simulations allow the yield/failure stress to be calculated as 2.45 ± 0.07 GPa for NU-1000-bip, nearly an order of magnitude higher than the $298 \pm 22\,$ MPa of NU-1000-ben. The load-displacement results from the corresponding simulations matched remarkably well with the experimentally measured load displacement behavior for NU-1000-bip, as seen in Figure 6c. The simulation matches less well for NU-1000-ben, which may be partly due to the NU-901 phase impurities disrupting the structure. Of note is that the simulated load-displacement response corresponding to NU-1000bip has a non-zero slope post-failure. This differs from what one might expect for an elasticperfectly plastic material, but it can be explained by examining the stress distribution within the particle seen in Figure 8. Three distinct zones can be seen in the particle: (1) red, corresponding to fully yielded material; (2) green, corresponding to material that is elastically strained; (3) blue, corresponding to material that has undergone minimal deformation. The non-zero loading slope post-failure is a result of the particle geometry; even after some of the material has yielded, there is other material further from the center that continues to deform elastically, resulting in a nonzero loading slope after yield.

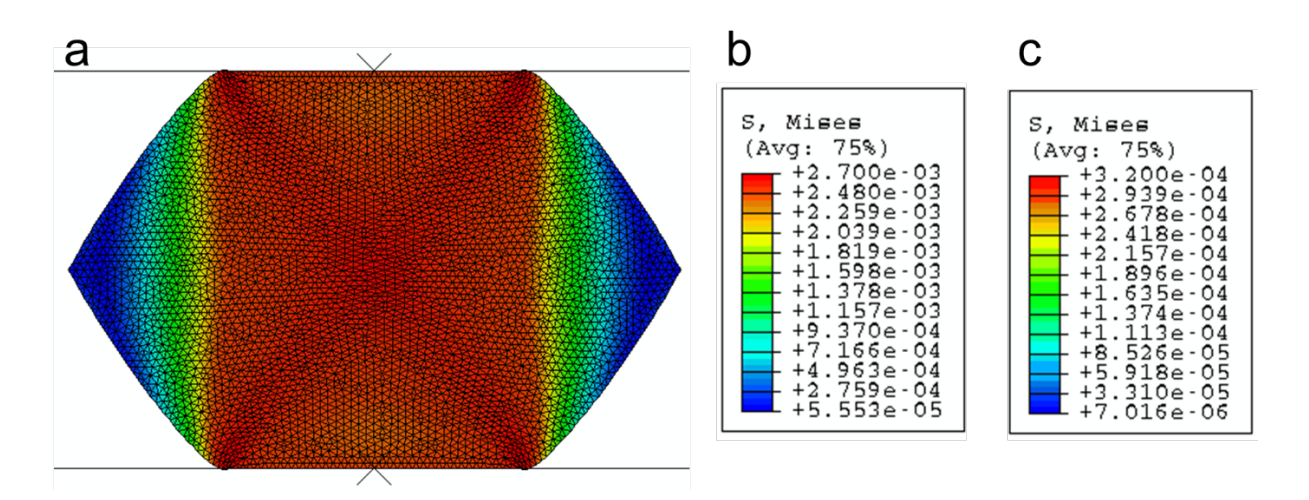


Figure 8. (a) The shape of the stress distribution at the point of failure assuming elastic–perfectly plastic behavior. Colors correspond to stress contours for (b) NU-1000-bip and (c) NU-1000-ben. Stresses are von Mises stresses with units of TPa. Yield stresses are 2.5 GPa and 300 MPa for NU-1000-bip and NU-1000-ben, respectively.

The hardness values of common MOFs have been reported to be in the range of 170–1300 MPa (**Table 1**). Converting these values of hardness to flow stresses using a Tabor factor (constraint factor) of 3 implies flow stress on the order of 60–430 MPa. These values are difficult to compare to the failure stresses from the compression tests in this study because of a difference in stress state. The stress state underneath a Berkovich indent is triaxial and spatially dependent, whereas uniaxial compression is expected to create a more homogeneous stress state. In addition, the Tabor factor assumes a constrained medium, an assumption which is difficult to confirm in a porous material such as a MOF. The uniaxial tests performed in this study are expected to be, in an idealized structure (**Figure 1a**), along the edge of a hexagonal structure connected by equilateral triangles, which are typically considered to be a strong shape. In order to deform the walls of the hexagonal pore of NU-1000, the highly conjugated, stiff linkers would likely need to bend. If they were to bend away from the hexagonal pore, they would bend into the equilateral triangle structure. Overall, there is minimal room for them to bend into the triangle structure before strongly

interacting with other deforming linkers. Altogether, the structure of the phase-pure NU-1000-bip allows for high mechanical strength. In contrast, the NU-901 phase in NU-1000-ben weakens the structure due to its easy deformability, resulting in a material with effective elastic modulus and yield/failure stress nearly an order of magnitude lower than the phase-pure material. Ultimately, the silica-infiltrated particles had similar elastic modulus as the phase-pure NU-1000-bip, but were able to withstand significantly higher loads and, therefore, represent the strongest form of the NU-1000 MOF.

4. CONCLUSION

The mechanical properties of phase-pure NU-1000, NU-901-containing NU-1000, and silica reinforced NU-1000 were investigated. As the NU-901 phase impurity in NU-1000 was removed through applying a different modulator, the particle morphology changed to a more uniform structure with a smoother surface, the effective elastic modulus increased from 3 GPa (NU-1000-ben) to 20 GPa (NU-1000-bip), and the yield/failure stress was increased from 300 MPa to 2.5 GPa. These results suggest that a uniform structure might be important for MOF materials to be robust. Silica reinforcement in the mesopores of NU-1000 (SiO_x(OH)_y@NU-1000) was found to increase the load at failure from 2000 μ N to 3000–4000 μ N. This result implies a possible modification method to escalate the mechanical properties of MOFs. This method might also be applicable to other MOF materials to enhance their mechanical properties.

ASSOCIATED CONTENT

Supporting Information

The Supporting Information is available free of charge on the ACS Publications website at DOI:

. . .

SEM images, mechanical data, N2 sorption, XRD, TGA, NMR and XRD data, atomic ratios from

SEM-EDS data, elemental mapping by STEM-EDS.

AUTHOR INFORMATION

Corresponding authors

*E-mail: a-stein@umn.edu, mara@umn.edu

ORCID

Andreas Stein: 0000-0001-8576-0727

Zhao Wang: 0000-0003-4940-6346

Kevin Schmalbach: 0000-0002-4824-9900

R. Lee Penn: 0000-0002-9610-9507

Notes

The authors declare no competing financial interest.

ACKNOWLEDGMENTS

Mechanical testing and sample characterization described in this work were primarily

supported by the MRSEC Program of the National Science Foundation under Award Number

30

DMR-2011401. Synthesis of the materials was supported as part of the Inorganometallic Catalysis Design Center, an Energy Frontier Research Center funded by the U.S. Department of Energy, Office of Science, Basic Energy Sciences under Award DE-SC0012702. Parts of this work were carried out in the Characterization Facility, University of Minnesota, which receives partial support from NSF through the MRSEC program. The authors acknowledge the Minnesota Supercomputing Institute (MSI) at the University of Minnesota for providing resources that contributed to the research results reported within this paper. We thank Antonia Antoniou at Georgia Institute of Technology for helpful discussions regarding finite element modeling, the Hupp and Farha groups from Northwestern University for providing H₄TBAPy linkers for the MOF synthesis, Dr. L. Chip Reisman for carrying out TGA measurements, and Yuan Sheng for carrying out ¹H NMR measurements.

REFERENCES

- 1. Zhou, H. C.; Long, J. R.; Yaghi, O. M. Introduction to Metal-Organic Frameworks. *Chem. Rev.* **2012**, *112*, 673-674.
- Furukawa, H.; Cordova, K. E.; O'Keeffe, M.; Yaghi, O. M. The Chemistry and Applications
 of Metal-Organic Frameworks. *Science* 2013, 341, 1230444.
- 3. Yuan, S.; Feng, L.; Wang, K.; Pang, J.; Bosch, M.; Lollar, C.; Sun, Y.; Qin, J.; Yang, X.; Zhang, P.; Wang, Q.; Zou, L.; Zhang, Y.; Zhang, L.; Fang, Y.; Li, J.; Zhou, H. C. Stable Metal–Organic Frameworks: Design, Synthesis, and Applications. *Adv. Mater.* **2018**, *30*, 1704303.
- 4. Howarth, A. J.; Liu, Y.; Li, P.; Li, Z.; Wang, T. C.; Hupp, J. T.; Farha, O. K. Chemical, Thermal and Mechanical Stabilities of Metal–Organic Frameworks. *Nat. Rev. Mater.* **2016**, *1*, 15018.

- Cambridge Structural Database (CSD) MOF Subset.
 https://sites.google.com/view/csdmofsubset/home (accessed May 14, 2020).
- 6. Altintas, C.; Avci, G.; Daglar, H.; Nemati Vesali Azar, A.; Erucar, I.; Velioglu, S.; Keskin, S. An Extensive Comparative Analysis of Two MOF Databases: High-Throughput Screening of Computation-Ready MOFs for CH₄ and H₂ Adsorption. *J. Mater. Chem. A* 2019, 7, 9593-9608.
- 7. Deng, H.; Grunder, S.; Cordova, K. E.; Valente, C.; Furukawa, H.; Hmadeh, M.; Gándara, F.; Whalley, A. C.; Liu, Z.; Asahina, S.; Kazumori, H.; O'Keeffe, M.; Terasaki, O.; Stoddart, J. F.; Yaghi, O. M. Large-Pore Apertures in a Series of Metal-Organic Frameworks. *Science* 2012, 336, 1018-1023.
- 8. Hönicke, I. M.; Senkovska, I.; Bon, V.; Baburin, I. A.; Bönisch, N.; Raschke, S.; Evans, J. D.; Kaskel, S. Balancing Mechanical Stability and Ultrahigh Porosity in Crystalline Framework Materials. *Angew. Chem. Int. Ed.* **2018**, *57*, 13780-13783.
- Krause, S.; Evans, J. D.; Bon, V.; Senkovska, I.; Iacomi, P.; Kolbe, F.; Ehrling, S.; Troschke, E.; Getzschmann, J.; Tobbens, D. M.; Franz, A.; Wallacher, D.; Yot, P. G.; Maurin, G.; Brunner, E.; Llewellyn, P. L.; Coudert, F. X.; Kaskel, S. Towards General Network Architecture Design Criteria for Negative Gas Adsorption Transitions in Ultraporous Frameworks. *Nat. Commun.* 2019, *10*, 3632.
- 10. Zhang, H.; Liu, X.; Wu, Y.; Guan, C.; Cheetham, A. K.; Wang, J. MOF-Derived Nanohybrids for Electrocatalysis and Energy Storage: Current Status and Perspectives. *Chem. Commun.* 2018, 54, 5268-5288.
- 11. Moghadam, P. Z.; Li, A.; Wiggin, S. B.; Tao, A.; Maloney, A. G. P.; Wood, P. A.; Ward, S.C.; Fairen-Jimenez, D. Development of a Cambridge Structural Database Subset: A

- Collection of Metal–Organic Frameworks for Past, Present, and Future. *Chem. Mater.* **2017**, 29, 2618-2625.
- 12. Rosi, N. L.; Eckert, J.; Eddaoudi, M.; Vodak, D. T.; Kim, J.; O'Keeffe, M.; Yaghi, O. M. Hydrogen Storage in Microporous Metal-Organic Frameworks. *Science* **2003**, *300*, 1127-1129.
- 13. Farha, O. K.; Yazaydin, A. O.; Eryazici, I.; Malliakas, C. D.; Hauser, B. G.; Kanatzidis, M. G.; Nguyen, S. T.; Snurr, R. Q.; Hupp, J. T. De Novo Synthesis of a Metal-Organic Framework Material Featuring Ultrahigh Surface Area and Gas Storage Capacities. *Nat. Chem.* 2010, 2, 944-948.
- 14. Seo, J. S.; Whang, D.; Lee, H.; Jun, S. I.; Oh, J.; Jeon, Y. J.; Kim, K. A Homochiral Metal–Organic Porous Material for Enantioselective Separation and Catalysis. *Nature* **2000**, *404*, 982-986.
- Kim, M.; Zhao, W.; Tsapatsis, M.; Stein, A. Three-Dimensionally Ordered Macroporous Mixed Metal Oxide as an Indicator for Monitoring the Stability of ZIF-8. *Chem. Mater.* 2020, 32, 3850-3859.
- 16. Wu, C.-D.; Hu, A.; Zhang, L.; Lin, W. A Homochiral Porous Metal—Organic Framework for Highly Enantioselective Heterogeneous Asymmetric Catalysis. J. Am. Chem. Soc. 2005, 127, 8940-8941.
- Mondloch, J. E.; Katz, M. J.; Isley Iii, W. C.; Ghosh, P.; Liao, P.; Bury, W.; Wagner, G. W.;
 Hall, M. G.; DeCoste, J. B.; Peterson, G. W.; Snurr, R. Q.; Cramer, C. J.; Hupp, J. T.; Farha,
 O. K. Destruction of Chemical Warfare Agents Using Metal–Organic Frameworks. *Nat. Mater.* 2015, *14*, 512-516.

- 18. Lan, A.; Li, K.; Wu, H.; Olson, D. H.; Emge, T. J.; Ki, W.; Hong, M.; Li, J. A Luminescent Microporous Metal–Organic Framework for the Fast and Reversible Detection of High Explosives. *Angew. Chem. Int. Ed.* 2009, 48, 2334-2338.
- 19. Chapman, K. W.; Halder, G. J.; Chupas, P. J. Pressure-Induced Amorphization and Porosity Modification in a Metal-Organic Framework. *J. Am. Chem. Soc.* **2009**, *131*, 17546-17547.
- 20. Su, Z.; Miao, Y.-R.; Zhang, G.; Miller, J. T.; Suslick, K. S. Bond Breakage under Pressure in a Metal Organic Framework. *Chem. Sci.* **2017**, *8*, 8004-8011.
- 21. Peterson, G. W.; DeCoste, J. B.; Glover, T. G.; Huang, Y.; Jasuja, H.; Walton, K. S. Effects of Pelletization Pressure on the Physical and Chemical Properties of the Metal–Organic Frameworks Cu₃(BTC)₂ and UiO-66. *Micropor. Mesopor. Mat.* **2013**, *179*, 48-53.
- 22. Dhainaut, J.; Avci-Camur, C.; Troyano, J.; Legrand, A.; Canivet, J.; Imaz, I.; Maspoch, D.; Reinsch, H.; Farrusseng, D. Systematic Study of the Impact of MOF Densification into Tablets on Textural and Mechanical Properties. *CrystEngComm* 2017, *19*, 4211-4218.
- 23. Moghadam, P. Z.; Rogge, S. M. J.; Li, A.; Chow, C.-M.; Wieme, J.; Moharrami, N.; Aragones-Anglada, M.; Conduit, G.; Gomez-Gualdron, D. A.; Van Speybroeck, V.; Fairen-Jimenez, D. Structure-Mechanical Stability Relations of Metal-Organic Frameworks Via Machine Learning. *Matter* 2019, 1, 219-234.
- 24. Sun, Y.; Hu, Z.; Zhao, D.; Zeng, K. Mechanical Properties of Microcrystalline Metal— Organic Frameworks (MOFs) Measured by Bimodal Amplitude Modulated-Frequency Modulated Atomic Force Microscopy. ACS Appl. Mater. Interfaces 2017, 9, 32202-32210.
- 25. Robison, L.; Drout, R. J.; Redfern, L. R.; Son, F. A.; Wasson, M. C.; Goswami, S.; Chen, Z.; Olszewski, A.; Idrees, K. B.; Islamoglu, T.; Farha, O. K. Designing Porous Materials to

- Resist Compression: Mechanical Reinforcement of a Zr-MOF with Structural Linkers. *Chem. Mater.* **2020**, *32*, 3545-3552.
- 26. Bundschuh, S.; Kraft, O.; Arslan, H. K.; Gliemann, H.; Weidler, P. G.; Wöll, C. Mechanical Properties of Metal-Organic Frameworks: An Indentation Study on Epitaxial Thin Films. *Appl. Phys. Lett.* **2012**, *101*, 101910.
- 27. Van de Voorde, B.; Ameloot, R.; Stassen, I.; Everaert, M.; De Vos, D.; Tan, J. C. Mechanical Properties of Electrochemically Synthesised Metal–Organic Framework Thin Films. *J. Mater. Chem. C* **2013**, *1*, 7716-7724.
- 28. Tan, J. C.; Bennett, T. D.; Cheetham, A. K. Chemical Structure, Network Topology, and Porosity Effects on the Mechanical Properties of Zeolitic Imidazolate Frameworks. *PNAS* 2010, 107, 9938-9943.
- Bahr, D. F.; Reid, J. A.; Mook, W. M.; Bauer, C. A.; Stumpf, R.; Skulan, A. J.; Moody, N. R.; Simmons, B. A.; Shindel, M. M.; Allendorf, M. D. Mechanical Properties of Cubic Zinc Carboxylate IRMOF-1 Metal-Organic Framework Crystals. *Phys. Rev. B* 2007, *76*, 184106.
- 30. Zeng, Z.; Tan, J. C. AFM Nanoindentation to Quantify Mechanical Properties of Nano- and Micron-Sized Crystals of a Metal—Organic Framework Material. ACS Appl. Mater. Interfaces 2017, 9, 39839-39854.
- 31. Hobday, C. L.; Marshall, R. J.; Murphie, C. F.; Sotelo, J.; Richards, T.; Allan, D. R.; Düren, T.; Coudert, F.-X.; Forgan, R. S.; Morrison, C. A.; Moggach, S. A.; Bennett, T. D. A Computational and Experimental Approach Linking Disorder, High-Pressure Behavior, and Mechanical Properties in UiO Frameworks. *Angew. Chem. Int. Ed.* **2016**, *55*, 2401-2405.

- 32. Tan, J. C.; Cheetham, A. K. Mechanical Properties of Hybrid Inorganic–Organic Framework Materials: Establishing Fundamental Structure–Property Relationships. *Chem. Soc. Rev.* **2011**, *40*, 1059-1080.
- 33. Tan, J. C.; Merrill, C. A.; Orton, J. B.; Cheetham, A. K. Anisotropic Mechanical Properties of Polymorphic Hybrid Inorganic–Organic Framework Materials with Different Dimensionalities. *Acta Mater.* 2009, 57, 3481-3496.
- 34. Tan, J. C.; Furman, J. D.; Cheetham, A. K. Relating Mechanical Properties and Chemical Bonding in an Inorganic–Organic Framework Material: A Single–Crystal Nanoindentation Study. *J. Am. Chem. Soc.* **2009**, *131*, 14252-14254.
- 35. Mondloch, J. E.; Bury, W.; Fairen-Jimenez, D.; Kwon, S.; DeMarco, E. J.; Weston, M. H.; Sarjeant, A. A.; Nguyen, S. T.; Stair, P. C.; Snurr, R. Q.; Farha, O. K.; Hupp, J. T. Vapor-Phase Metalation by Atomic Layer Deposition in a Metal-Organic Framework. *J. Am. Chem. Soc.* **2013**, *135*, 10294-10297.
- 36. Ikuno, T.; Zheng, J.; Vjunov, A.; Sanchez-Sanchez, M.; Ortuño, M. A.; Pahls, D. R.; Fulton, J. L.; Camaioni, D. M.; Li, Z.; Ray, D.; Mehdi, B. L.; Browning, N. D.; Farha, O. K.; Hupp, J. T.; Cramer, C. J.; Gagliardi, L.; Lercher, J. A. Methane Oxidation to Methanol Catalyzed by Cu-Oxo Clusters Stabilized in NU-1000 Metal-Organic Framework. *J. Am. Chem. Soc.* 2017, 139, 10294-10301.
- 37. Li, Z.; Peters, A. W.; Platero-Prats, A. E.; Liu, J.; Kung, C.-W.; Noh, H.; DeStefano, M. R.; Schweitzer, N. M.; Chapman, K. W.; Hupp, J. T.; Farha, O. K. Fine-Tuning the Activity of Metal–Organic Framework-Supported Cobalt Catalysts for the Oxidative Dehydrogenation of Propane. J. Am. Chem. Soc. 2017, 139, 15251-15258.

- 38. Desai, S. P.; Ye, J.; Zheng, J.; Ferrandon, M. S.; Webber, T. E.; Platero-Prats, A. E.; Duan, J.; Garcia-Holley, P.; Camaioni, D. M.; Chapman, K. W.; Delferro, M.; Farha, O. K.; Fulton, J. L.; Gagliardi, L.; Lercher, J. A.; Penn, R. L.; Stein, A.; Lu, C. C. Well-Defined Rhodium-Gallium Catalytic Sites in a Metal-Organic Framework: Promoter-Controlled Selectivity in Alkyne Semihydrogenation to E-Alkenes. *J. Am. Chem. Soc.* 2018, 140, 15309-15318.
- 39. Liu, J.; Ye, J.; Li, Z.; Otake, K.-i.; Liao, Y.; Peters, A. W.; Noh, H.; Truhlar, D. G.; Gagliardi, L.; Cramer, C. J.; Farha, O. K.; Hupp, J. T. Beyond the Active Site: Tuning the Activity and Selectivity of a Metal–Organic Framework-Supported Ni Catalyst for Ethylene Dimerization. *J. Am. Chem. Soc.* **2018**, *140*, 11174-11178.
- 40. Slater, A. G.; Cooper, A. I. Porous Materials. Function-Led Design of New Porous Materials. *Science* **2015**, *348*, aaa8075.
- Malonzo, C. D.; Shaker, S. M.; Ren, L.; Prinslow, S. D.; Platero-Prats, A. E.; Gallington, L. C.; Borycz, J.; Thompson, A. B.; Wang, T. C.; Farha, O. K.; Hupp, J. T.; Lu, C. C.; Chapman, K. W.; Myers, J. C.; Penn, R. L.; Gagliardi, L.; Tsapatsis, M.; Stein, A. Thermal Stabilization of Metal–Organic Framework-Derived Single-Site Catalytic Clusters through Nanocasting. *J. Am. Chem. Soc.* 2016, *138*, 2739-2748.
- 42. Zhao, W.; Wang, Z.; Malonzo, C. D.; Webber, T. E.; Platero-Prats, A. E.; Sotomayor, F.; Vermeulen, N. A.; Wang, T. C.; Hupp, J. T.; Farha, O. K.; Penn, R. L.; Chapman, K. W.; Thommes, M.; Stein, A. Extending the Compositional Range of Nanocasting in the Oxozirconium Cluster-Based Metal—Organic Framework NU-1000—a Comparative Structural Analysis. *Chem. Mater.* **2018**, *30*, 1301-1315.

- 43. Wang, T. C.; Vermeulen, N. A.; Kim, I. S.; Martinson, A. B. F.; Stoddart, J. F.; Hupp, J. T.; Farha, O. K. Scalable Synthesis and Post-Modification of a Mesoporous Metal-Organic Framework Called NU-1000. *Nat. Protoc.* **2015**, *11*, 149-162.
- 44. Cavka, J. H.; Jakobsen, S.; Olsbye, U.; Guillou, N.; Lamberti, C.; Bordiga, S.; Lillerud, K. P. A New Zirconium Inorganic Building Brick Forming Metal Organic Frameworks with Exceptional Stability. *J. Am. Chem. Soc.* 2008, *130*, 13850-13851.
- 45. Deria, P.; Mondloch, J. E.; Tylianakis, E.; Ghosh, P.; Bury, W.; Snurr, R. Q.; Hupp, J. T.; Farha, O. K. Perfluoroalkane Functionalization of NU-1000 Via Solvent-Assisted Ligand Incorporation: Synthesis and CO₂ Adsorption Studies. *J. Am. Chem. Soc.* 2013, 135, 16801-16804.
- 46. Desai, S. P.; Malonzo, C. D.; Webber, T.; Duan, J.; Thompson, A. B.; Tereniak, S. J.;
 DeStefano, M. R.; Buru, C. T.; Li, Z.; Penn, R. L.; Farha, O. K.; Hupp, J. T.; Stein, A.; Lu,
 C. C. Assembly of Dicobalt and Cobalt-Aluminum Oxide Clusters on Metal-Organic
 Framework and Nanocast Silica Supports. *Faraday Discuss.* 2017, 201, 287-302.
- 47. Garibay, S. J.; Iordanov, I.; Islamoglu, T.; DeCoste, J. B.; Farha, O. K. Synthesis and Functionalization of Phase-Pure NU-901 for Enhanced CO₂ Adsorption: The Influence of a Zirconium Salt and Modulator on the Topology and Phase Purity. *CrystEngComm* 2018, 20, 7066-7070.
- 48. Webber, T. E.; Liu, W.-G.; Desai, S. P.; Lu, C. C.; Truhlar, D. G.; Penn, R. L. Role of a Modulator in the Synthesis of Phase-Pure NU-1000. *ACS Appl. Mater. Interfaces* **2017**, *9*, 39342-39346.

- 49. Tsuruoka, T.; Furukawa, S.; Takashima, Y.; Yoshida, K.; Isoda, S.; Kitagawa, S. Nanoporous Nanorods Fabricated by Coordination Modulation and Oriented Attachment Growth. *Angew. Chem. Int. Ed.* **2009**, *48*, 4739-4743.
- 50. Rosnes, M. H.; Nesse, F. S.; Opitz, M.; Dietzel, P. D. C. Morphology Control in Modulated Synthesis of Metal-Organic Framework CPO-27. *Micropor. Mesopor. Mat.* **2019**, *275*, 207-213.
- 51. Malonzo, C. D.; Wang, Z.; Duan, J.; Zhao, W.; Webber, T. E.; Li, Z.; Kim, I. S.; Kumar, A.; Bhan, A.; Platero-Prats, A. E.; Chapman, K. W.; Farha, O. K.; Hupp, J. T.; Martinson, A. B. F.; Penn, R. L.; Stein, A. Application and Limitations of Nanocasting in Metal-Organic Frameworks. *Inorg. Chem.* 2018, *57*, 2782-2790.
- 52. Dongare, M. K.; Singh, P.; Moghe, P. P.; Ratnasamy, P. Synthesis, Characterization, and Catalytic Properties of [Zr]-ZSM-5. *Zeolites* **1991**, *11*, 690-693.
- 53. Lucovsky, G.; Jr., G. B. R. Microscopic Model for Enhanced Dielectric Constants in Low Concentration SiO₂-Rich Noncrystalline Zr and Hf Silicate Alloys. *Appl. Phys. Lett.* **2000**, 77, 2912-2914.
- 54. Miao, Y. R.; Su, Z.; Suslick, K. S. Energy Storage During Compression of Metal-Organic Frameworks. *J. Am. Chem. Soc.* **2017**, *139*, 4667-4670.
- 55. Tabor, D., The Hardness of Metals. Oxford University Press: London, 1951.

For Table of Contents Only:

